

## CRYSTAL STRUCTURE AND MAGNETIC PROPERTIES OF SrLaLiTeO<sub>6</sub> DOUBLE PEROVSKITES

M. Z. M. HALIZAN<sup>a</sup>, A. K. YAHYA<sup>a</sup>, N. B. IBRAHIM<sup>b</sup>, N. IBRAHIM<sup>a</sup>,  
Z. MOHAMED<sup>a,\*</sup>

<sup>a</sup>Faculty of Applied Sciences, Universiti Teknologi MARA, 40450, Shah Alam, Selangor, Malaysia

<sup>b</sup>Faculty of Science and Technology, Universiti Kebangsaan Malaysia, 43600, Bangi, Selangor, Malaysia

In this study, SrLaLiTeO<sub>6</sub> compound was synthesized using solid-state method, and its morphology and magnetic properties were investigated for the first time. The Rietveld refinement of the X-ray diffraction data showed that the compound crystallized in monoclinic symmetry ( $P2_1/n$  space group) and the formation of Li–O–Te bonds in the compound were confirmed using infrared spectroscopy. The morphological study exhibited rough grain formation on the compound. AC magnetization measurement at different frequencies in the range of 200–500 Hz showed that this compound had magnetic paramagnetic transition to spin glass (SG) as the temperature decreased from room temperature to 20 K. For the SG value,  $p = 0.13$  was calculated at the temperature range 70–80 K, which indicates that this compound may possess cluster glass or superparamagnetic properties instead of conventional SG.

(Received December 9, 2019; Accepted July 31, 2020)

**Keywords:** Double perovskites, SrLaLiTeO<sub>6</sub>, Structural, Rietveld, Magnetic, Spin glass

### 1. Introduction

Research on perovskites have been conducted extensively due to its promising abilities, such as magnetic, electrical, optical or mechanical properties [1-3]. The main characteristics of these compounds are ionic conductivity, colossal magnetoresistance, ferroelectric and ferromagnetic abilities. Owing to these abilities, perovskites can be deployed in many applications such as sensors [4,5], capacitors [6], microwave resonators [7] and magnetic memory components [8].

Double perovskite oxides introduced an ordered rock salt-like arrangement of corner-sharing BO<sub>6</sub> and B'O<sub>6</sub> units in the crystal structure. Double perovskite oxides essentially comprise A<sub>2</sub>BB'O<sub>6</sub> or AA'BB'O<sub>6</sub> configuration, where A or A' is an alkaline- or rare-earth metal in groups I or II, while B and B' are transition metals. These configurations were derived from ABO<sub>3</sub> ternary perovskites, where 6 out of the 12 A-site cations and 6 B-site cations were replaced by appropriate A' and B' cations, respectively. Double perovskite with the general configuration of A<sub>2</sub>BB'O<sub>6</sub> exhibited a wide range of interesting properties from theoretical points of view, including magnetic property which is also applied to uncommon Te<sup>6+</sup>-based double perovskites. For instance, structural and magnetic property of Sr<sub>2</sub>CoTeO<sub>6</sub> compounds investigated and it was reported that Sr<sub>2</sub>CoTeO<sub>6</sub> compound exhibits  $P2_1/n$  monoclinic structure and AFM ordering [9, 10] or very small FM property with T<sub>N</sub> at 15 K. The relatively high T<sub>N</sub> and lower ordered moment for Sr<sub>2</sub>CoTeO<sub>6</sub> (5.48 mB f.u.<sup>-1</sup>) can be correlated with the A-site ions which affecting the charge in Co-O bonds indirectly [9]. Structural and magnetic studies on Sr<sub>2</sub>Co<sub>1-x</sub>Mg<sub>x</sub>TeO<sub>6</sub> compounds were done where they displayed  $P2_1/n$  monoclinic and  $I2/m$  tetragonal structure at low doping and high doping, respectively. Furthermore, oppression towards FM property occurred in this perovskite with increment of dopant concentrations at Co-sites [11].

Besides, attentions have been focused to AA'BB'O<sub>6</sub> double perovskites too. This kind of perovskites exhibits simultaneous layered ordering of A-site cations and rock salt ordering of B-

\* Corresponding author: zakiah626@uitm.edu.my

site cations. Recently, Amrithakrishnan et al. [12] discussed SrLaLiTeO<sub>6</sub> compound and this compound possesses  $P2_1/n$  monoclinic structure and 1:1 B-site ordering of Te<sup>6+</sup> and Li<sup>+</sup> cations. These results were supported by works of Lal et al. [13] and Lopez et al. [14]. Study of magnetic property of this compound is still unavailable in literature. Thus, we aim to understand the structure-magnetism correlation mechanism in SrLaLiTeO<sub>6</sub>.

## 2. Experimental

The polycrystalline powders of SrLaLiTeO<sub>6</sub> were synthesized using a solid-state reaction method. High-purity ( $\geq 99.99\%$ ) strontium carbonate (SrCO<sub>3</sub>), lithium carbonate (Li<sub>2</sub>CO<sub>3</sub>), lanthanum oxide (La<sub>2</sub>O<sub>3</sub>) and tellurium dioxide (TeO<sub>2</sub>) powders were used as raw materials. The chemical powders were mixed at stoichiometric ratios with a total mass of 5 g. Then, the samples were ground in agate mortar by pestle for 1 h to achieve good homogeneity. After the grinding process, the mixed powder sample was pressed into a pellet at the pressure range of 4–5 KPa by using hydraulic press. Then, the pellet was placed on an alumina crucible and calcinated in a box furnace at 850 °C for 10 h, with heating rate of 15 °C/min and cooling rate of 1 °C/min. The crystal structure of the sample was analyzed by XRD measurement in a PANanalytical model Xpert PRO MPD diffractometer equipped with a Cu K $\alpha$  source. EXPGUI software [15,16] was used for Rietveld refinement [17] prior as visualized in the VESTA program. Peak shape was modeled by pseudo-Voigt function that was refined together with cell parameter, scale factor, zero factor, and background function. The infrared (IR) reflectance spectra were recorded in Fourier transform IR (FTIR)-Raman Drift Nicolet 6700 equipment ranging from 400 cm<sup>-1</sup> to 1500 cm<sup>-1</sup>. As preparation, the sample needs to be mixed thoroughly with KBr before the FTIR characterization. Morphology study was conducted via Field-emission Scanning Electron Microscopy (FESEM) characterization by using SU 8000 (Hitachi, Japan). The grain size was measured using ImageJ software. Magnetic study was performed by AC susceptibility measurement using a Signal Recovery 7265 lock-in amplifier from 300 K to 20 K, with frequencies ranging from 200 Hz to 500 Hz at 1 Oe.

## 3. Results and discussion

Fig. 1 shows the refined XRD data of SrLaLiTeO<sub>6</sub> by the Rietveld refinement method. The compound formed in a single phase. The obtained reliability ( $\chi^2$ ) was 1.258, and the refined lattice parameters were  $a = 5.631 \text{ \AA}$ ,  $b = 5.598 \text{ \AA}$ ,  $c = 7.931 \text{ \AA}$  whereas  $\alpha = 90^\circ$ ,  $\beta = 90^\circ$  and  $\gamma = 90^\circ$ . The obtained unit cell volume of this sample was  $249.9 \text{ \AA}^3$ . Good agreement between observed and calculated interplanar spacings (d-values) indicated that this compound was crystallized in a monoclinic structure with a  $P2_1/n$  space group structure. The parameters obtained from this refinement are presented in Table 1. As shown in this table, six O<sup>2-</sup> were located around each Te<sup>6+</sup> and Li<sup>+</sup> to form an octahedral-like structure from the  $ab$  plane, while Sr<sup>2+</sup> and La<sup>3+</sup> tended to merge (fill the same occupancy) and be placed between these Te(Li)O<sub>6</sub> octahedral layers, as presented in Figure 2. This compound was arranged in a monoclinic structure with a rock salt lattice of the corner-shared octahedra of TeO<sub>6</sub>, with Sr and La cations positioned in the cubic 12-fold coordination sites. Li and Te did not merge on the B sites observed in the single-crystal X-ray data due to the large charge difference between the Li<sup>+</sup> and Te<sup>6+</sup> cations. The locations of Sr<sup>2+</sup> and La<sup>3+</sup> were at (0.497, 0.506, 0.253), while Li<sup>+</sup> was at (0.5, 0, 0) and Te<sup>6+</sup> at (0, 0.5, 0), as calculated by the following tolerance factor formula:

$$\tau = \frac{\frac{R_a + R_{a'}}{2} + R_o}{\sqrt{2}(\frac{R_b + R_{b'}}{2} + R_o)} \quad (1)$$

where  $R_a$  and  $R_{a'}$  represent radii of A-site atoms (Sr and La),  $R_b$  and  $R_{b'}$  represent radii of B-site atoms (Li and Te) and  $R_o$  represents radius of oxygen atom (O), respectively. For an ideal cubic

structure,  $\tau$  must be equal to 1. If the A-site cation was extremely small, or the B-site cation was extremely large, the structure was distorted, with the tilting occurrence of the B and B' octahedra, thereby decreasing the crystal symmetry of the double perovskite from cubic (the perfect cube) to decrease symmetry configurations until monoclinic symmetry was achieved; this result was indicated by the deviation of the tolerance factor further from  $\tau = 1$ . For this compound, the obtained value was 0.961 with  $\text{Sr}^{2+}$  of 1.44 Å [CN:12],  $\text{La}^{3+}$  of 1.36 Å [CN:12],  $\text{Li}^+$  of 0.76 Å [CN:6],  $\text{Te}^{6+}$  of 0.56 Å [CN:6], and  $\text{O}^{2-}$  of 1.40 Å [CN:6] [18] in agreement with reported result [12]. The relatively small sizes of  $\text{Sr}^{2+}$  and  $\text{La}^{3+}$  resulted in a tolerance factor of  $<0.99$ . The value of the octahedra tilting distortion angle was calculated based on the following equation:

$$\phi = \frac{180-\theta}{2} \quad (2)$$

where  $\theta$  represents the average (Li–O–Te) bond angles [19]. The value that calculated for this sample was  $9.6^\circ$ . The average bond distance of Sr/La–O was 2.817(2) Å. The tilting caused the bond angles between octahedral B sites Li–O<sub>1</sub>–Te, Li–O<sub>2</sub>–Te, and Li–O<sub>3</sub>–Te to be  $155.0(2)^\circ$ ,  $160.3(1)^\circ$  and  $167.1(7)^\circ$ , respectively. Meanwhile, the bond distances of Li–O and Te–O were 2.095(5) Å and 1.934(5) Å, respectively, where 2 equidistance bonds for every plane O in Te–O and Li–O bonds. Li–O<sub>1</sub>, Li–O<sub>2</sub>, and Li–O<sub>3</sub> bonds had 2.127(8) Å, 2.091(6) Å and 2.066(1) Å respectively. Meanwhile, Te–O<sub>1</sub>, Te–O<sub>2</sub>, and Te–O<sub>3</sub> had 1.939(7) Å, 1.939(6) Å and 1.925(1) Å, respectively. These values showed that tilting caused the structural lattice distortion of the B-site orthorhombic structure as they have different lengths in each Li/Te–O bonds in every plane. The average bond distances of Li–O were longer than those of Te–O, which agreed with the result that  $\text{Li}^+$  (0.76 Å) had a larger ionic radius than  $\text{Te}^{6+}$  (0.56 Å). The degree of cation ordering was also calculated from equation comprising long-range order parameter as follows [20]:

$$LRO = (2(occ)_M - 1) \times 100\% \quad (3)$$

where  $(occ)_M$  is the fractional occupancy of the  $\text{Li}^+$  or  $\text{Te}^{6+}$  cations in the octahedral structure of the B sites or  $\text{Sr}^{2+}$  or  $\text{La}^{3+}$  in the A sites that are predominantly occupied by this cation. The obtained value of LRO in the B sites was 100% as the fractional occupancy of  $\text{Li}^+$  or  $\text{Te}^{6+}$  cations was 1 from Rietveld refinement because no doped ions were observed in these sites. The long-range ordering in this compound was referred to as Li–O–Te–O–Li.

The crystallite size, D, was calculated using the following Scherrer equation [21]:

$$D = \frac{K\lambda}{\beta(\theta) \cos \theta} \quad (4)$$

where  $K$  is the constant (0.94),  $\lambda$  is the wavelength of XRD (1.5405 Å),  $\beta$  is the full width at half maximum, and  $\theta$  is the angle of peak of XRD. The calculated D in this compound was 18 nm. As D depended on the nucleation rate of the compound, the D value that was obtained for this compound was most probably due to the relatively low calcinating temperature at 850 °C for 10 h. Thus, the nucleation rate would be slow, thereby resulting in fine crystallite. Then, this process decreased the surface tension of the compound.

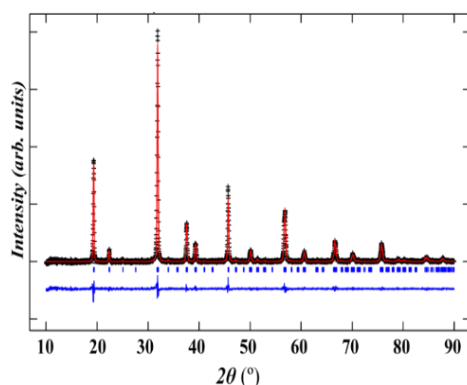


Fig. 1. Rietveld refinement of X-ray diffraction pattern  $\text{SrLaLiTeO}_6$ . Red crosses lines are observed data, the black solid line is the calculated pattern and the blue solid line is the difference. Blue tick marks indicate the allowed Bragg reflections for  $\text{SrLaLiTeO}_6$ .

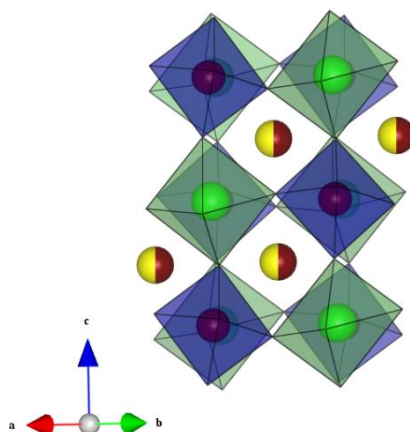


Fig. 2. Visual image of refined XRD of  $\text{SrLaLiTeO}_6$  from  $ac$  plane where yellow, red atoms indicate  $\text{Sr}^{2+}$  and  $\text{La}^{3+}$  cation, respectively, while purple, green atoms indicate  $\text{Te}^{6+}$  and  $\text{Li}^+$  cation, respectively.

Table 1. Lattice parameters, unit cell volume, calculated tilting angle ( $\phi$ ), calculated crystallite size ( $D$ ), good fitness, bond angles and bond lengths of  $\text{SrLaLiTeO}_6$  as obtained from Rietveld refinement.

Lattice parameters		Bond lengths ( $\text{\AA}$ )	
$a$ ( $\text{\AA}$ )	5.631	$\text{Li-O}_1(\times 2)$	2.127(8)
$b$ ( $\text{\AA}$ )	5.598	$\text{Li-O}_2(\times 2)$	2.091(6)
$c$ ( $\text{\AA}$ )	7.931	$\text{Li-O}_3(\times 2)$	2.066(1)
$\alpha$	90.00°	Ave. $\langle \text{Li-O} \rangle$	2.095(5)
$\beta$	90.03°	$\text{Te-O}_1(\times 2)$	1.939(7)
$\gamma$	90.00°	$\text{Te-O}_2(\times 2)$	1.939(6)
Unit cell volume, $V$ ( $\text{\AA}^3$ )		$\text{Te-O}_3(\times 2)$	1.925(1)
249.9		Ave. $\langle \text{Te-O} \rangle$	1.934(5)
Tilting angle, $\phi$		Ave. $\langle \text{Sr/La-O} \rangle$	2.817(2)
9.60°		Ave. $\langle \text{Sr-Sr} \rangle$	3.969(1)
Fit Goodness		Ave. $\langle \text{La-La} \rangle$	3.969(1)
$\chi^2$	1.21	Bond angles (°)	
$R_p$ (%)	7.90	$\text{Li-O}_1\text{-Te}$	155.1(2)
$R_{wp}$ (%)	10.38	$\text{Li-O}_2\text{-Te}$	160.3(1)
Crystallite Size, $D$		$\text{Li-O}_3\text{-Te}$	167.1(7)
18 nm			

Fig 3 shows that the FTIR result of SrLaLiTeO<sub>6</sub> with substantial ambient peaks was in the range of 400–1500 cm<sup>-1</sup>. The emergence of peaks with medium intensities at 455, 491, 495, 473, 509, 517, and 521 cm<sup>-1</sup> can be assigned to antisymmetric stretching vibrations ( $\nu_1$ ) in Te(Li)O<sub>6</sub> octahedra between Te–O–Li bonds. Meanwhile, the strong peaks at 641, 660, 677, 693, 711, 722, 727, 733, 745, and 757 cm<sup>-1</sup> can be assigned to the symmetric stretching vibration ( $\nu_2$ ) of the Te(Li)O<sub>6</sub> octahedra between Te–O–Li bonds [22-26]. An observable weak peak was observed at 870 cm<sup>-1</sup>, which was due to external mode other than Te(Li)O<sub>6</sub> octahedra. A feeble peak at 1427 cm<sup>-1</sup> was most probably due to the adsorbed moisture in the sample during FTIR run preparation.

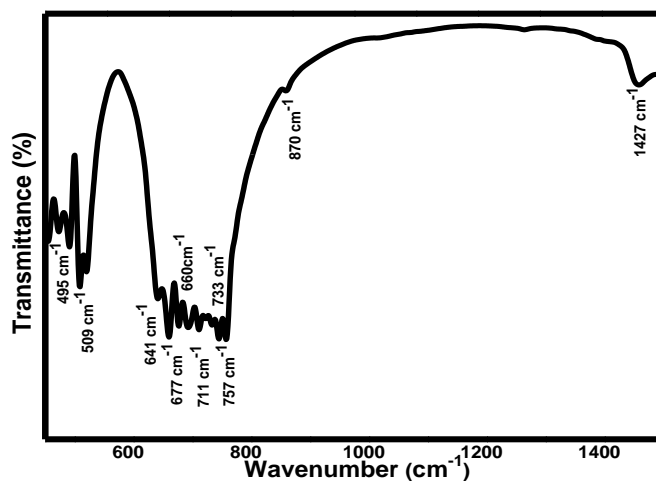


Fig. 3. FTIR spectrum of SrLaLiTeO<sub>6</sub>.

Fig. 4 exhibits the FESEM images with 5 and 10 K magnifications with EDX results possessing elements present in the sample. The image with 5 K magnification proved that this compound had grains that were discerned, rough, and had inhomogeneous characteristics with almost the same shape distribution. Meanwhile, 10 K magnification image illustrated that this compound had poor connectivity between grains. Similar size distribution of grains observed from this FESEM image. However, these grains formed the agglomerates. The measured size of agglomerates formed by these fine grains were in the range of 0.2–1.2  $\mu\text{m}$ . Due to the small size of crystallite, the sliding process between these grains can be frequent as there were lots of amorphous spaces between grains. However, the sliding process can be reduced with the formation of agglomerates [21]. The EDX graph showed that Sr, La, Te, Li and O elements existed in the sample in accordance with the stoichiometric chemical formula (not shown).

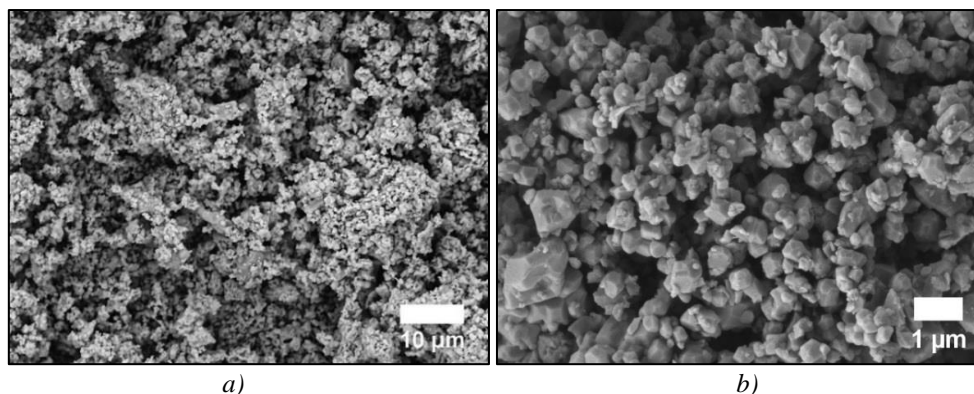


Fig. 4. FESEM images with (a) 5K magnification and (b) 10K magnification of SrLaLiTeO<sub>6</sub>.

As shown in Fig. 5a, that is, the graph of the real component of AC susceptibility,  $x'$  versus  $T$  showed the presence of peaks, which exhibited magnetic phase transition. This phenomenon was accompanied by the presence of peaks from the graph of the imaginary component of AC susceptibility,  $x''$  versus  $T$  in Figure 5b. The former graph showed frequency-dependent peaks, with shifted toward high temperatures from approximately 70 K to 72 K, as the frequency increased from 300 Hz to 500 Hz. Meanwhile, Fig. 5b shows the frequency-dependent peaks, which showed an upward shift at approximately 76 K to 79 K with increasing frequency. The  $x'$  susceptibility peaks decreased when frequency increased, while the height of the  $x''$  peaks was enhanced as frequency increased. Table 2 shows the peak temperatures obtained at each frequency for the  $x'$  and  $x''$  components.

To analyze the magnetic property further, we plotted the  $1/x'$  versus temperature plot for all frequencies. The inset of Fig. 5a shows the  $1/x'$  versus temperature plot for the samples at 300 Hz. As shown in this plot, the plot followed Curie law behavior when temperature decreased till 130 K prior deviation upward as temperatures further decreased. The plots for each frequency (300–500 Hz) exhibited the same trend and shape. For 400 and 500 Hz, the Curie law behavior was followed until the temperature decreased to 116 K and 119 K, respectively (not shown in the figure).  $T_c$  of each frequency included in Table 2.

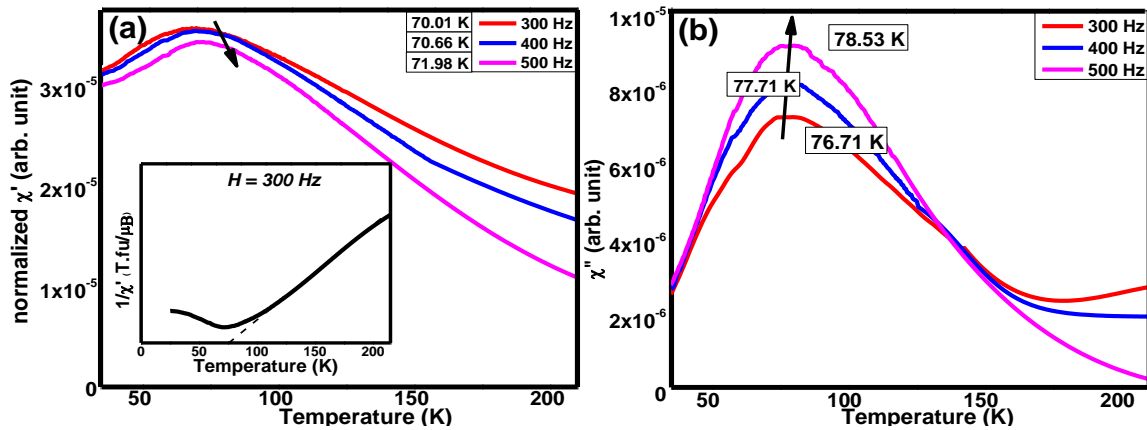


Fig. 5. (a) Real ( $x'$ ) and (b) imaginary ( $x''$ ) parts of AC susceptibility characterization of  $\text{SrLaLiTeO}_6$ . Inset of (a)  $1/x'$  graph from  $x'$  susceptibility.

Table 2. Freezing temperatures,  $T_f$  and Curie temperatures,  $T_c$  and maximum temperature,  $T_{max}$  at all frequencies in  $x'$ ,  $1/x'$  and  $x''$  component of ac susceptibility.

Real component, $x'$		Inverse of real component, $1/x'$		Imaginary component, $x''$	
Frequencies (Hz)	Freezing temperatures, $T_f$ (K)	Frequencies (Hz)	Curie temperatures, $T_c$ (K)	Frequencies (Hz)	Maximum temperatures, $T_{max}$ (K)
300	70	300	71	300	77
400	71	400	73	400	78
500	72	500	75	500	79

#### 4. Discussion

From XRD study, the average value of B-site atoms' bond distances and angles in  $\text{SrLaLiTeO}_6$  was between  $\text{Ca}_2\text{CoTeO}_6$  and  $\text{Sr}_2\text{CoTeO}_6$  compounds that were studied by other researchers. This result was attributed to the fact that  $\text{SrLaLiTeO}_6$  consisted of  $\text{Sr}^{2+}$  (1.44 Å) and  $\text{La}^{3+}$  (1.36 Å) ions in its A sites compared with  $\text{Ca}_2\text{CoTeO}_6$  possessing small  $\text{Ca}^{2+}$  ions and  $\text{Sr}_2\text{CoTeO}_6$  with large  $\text{Sr}^{2+}$  ions. This compound structure was comparable to other reports

regarding  $\text{TeO}_6$  double perovskite materials [10,11]. The octahedra tilt angle in this compound was a consequence of the presence of  $\text{Sr}^{2+}$  and  $\text{La}^{3+}$  size on A sites because octahedra tilt was needed to optimize the interatomic distance between A-site atoms with O (Sr/La–O) bonds. From FTIR study, the presence of  $\nu_1$  and  $\nu_2$  vibrations, we can confirm the formation of  $\text{Te}(\text{Li})\text{O}_6$  octahedra, which is the “fingerprint” of this compound. Thus, this compound was formed well, as visualized through Rietveld refinement method.

From AC susceptibility study, the deviation of graph from Curie’s law indicated that the sample demonstrated paramagnetic (PM) behavior above  $T_c$  before the transition into a different magnetic phase below  $T_c$  at each frequency. In the PM region, as the temperature decreased, the lattice scattering decreased and dipoles can easily align according to the external magnetic field. This result explained the PM behavior of  $x'$  within the range of the temperatures mentioned. Moreover, decrement in  $x'$  susceptibility (Figure 5a) below  $T_c$  may be due to the presence of the AFM spins or presence of an SG state. However, the shifting of the  $x'$  peak at different frequency supports the presence of SG behavior where the temperature of the susceptibility peak represented the freezing temperature ( $T_f$ ), which is almost the same as  $T_c$ . This suggesting that the transition from PM to SG occurs almost instantaneously. The temperature decreased below  $T_f$  and magnetic dipoles started to freeze, halting the alignment with external field  $H$ . The intensity of the  $x'$  susceptibility decreased as frequency increased, thereby indicating SG behavior [27].

The shift of the  $x'$  (T) peaks in  $x'$  against T graph was also reflected in the  $x''$  against T graph where the maximum temperature ( $T_{max}$ ) also shifted, and  $x''$  susceptibility decreased below  $T_{max}$ . Meanwhile, the intensity of  $x''$  (T) peaks, which were enhanced as the frequency increased, also supported the suggestion of the SG behavior below  $T_f$  [28].

To analyze the SG behavior further, we calculated the value of the shift in  $T_f$  per frequency decade,  $p$  from the  $x'$  plot (Fig. 5a). The shift was defined as follows [29]:

$$p = \frac{\left(\frac{\Delta T_f}{T_f}\right)}{\Delta \log f} \quad (5)$$

which was 0.13 for the present study. For a high value compared with the conventional SG value in the range of 0.01–0.05 [30], this value may suggest the presence of cluster glass (CG) interaction, small frustrated regions similar to CG, or even superparamagnets (SPM) property instead of conventional SG. Further characterizations are needed to confirm the property of this compound further, that is, whether it possesses CG or SPM characteristics.

As shown in Fig. 5a, the flat curve at further low temperature below  $T_f$  indicated the possible presence of the ferromagnetic phase. This occurrence was still unclear because further characterizations are needed to verify the presence of FM. Although no unpaired spin was expected for  $\text{SrLaLiTeO}_6$ , defects in the form of oxygen vacancies may be responsible for the presence of spin glass or other type of magnetism for the compound [31]. This kind of occurrence was the case in  $\text{ZrO}_2$  [32], where oxygen vacancies in the nonmagnetic compound was responsible for the existence of the weak ferromagnetic property. Similarly, for  $\text{SrTiO}_3$ , FM and SG emerged when the oxygen deficiencies value increased in this compound [33].

## 5. Conclusion

$\text{SrLaLiTeO}_6$  compound was prepared by using solid-state method. The structural, morphology and magnetic properties of this compound were investigated by XRD, FESEM, FTIR spectra and magnetic AC susceptibility techniques.  $\text{SrLaLiTeO}_6$  crystallizes in  $P2_1/n$  lattice structure and the formation of Li/Te-O octahedra were confirmed by FTIR characterization. This compound exhibited rough and low connected microstructures of the sample with calculated average grain size of 18 nm. For AC susceptibility characterization, this sample showed PM to SG/CG/superparamagnetic transition as the temperature decreased. Further research is needed to confirm the latter property.

## Acknowledgements

The authors would like to acknowledge the financial support by Ministry of Education Malaysia (MOHE) and Universiti Teknologi MARA (UiTM), Malaysia through the Fundamental Research Grant Scheme (FRGS) (Grant No. 600-IRMI/FRGS 5/3 (311/2019) and Supervisory Incentive Grant (Grant No. 600-IRMI 5/3/GIP-074/2019).

## References

- [1] A. S. Bhalla, G. Ruyan Guo, R. Rustum, *Materials Research Innovations* **4**(1), (2000).
- [2] M. Hadadian, J. P. Correa- Baena, E. K. Goharshadi, A. Ummadisingu, J. Y. Seo, J. Luo, S. Gholipour, S. M. Zakeeruddin, M. Saliba, A. Abate, M. Grätzel, *Advanced Materials* **28**(39), (2016).
- [3] C. Lan, S. Zhao, T. Xu, J. Ma, S. Hayase, T. Ma, *Journal of Alloys and Compounds* **655**, (2016).
- [4] W. Xu, F. Li, Z. Cai, Y. Wang, F. Luo, X. Chen, *Journal of Materials Chemistry C* **4**(41), (2016).
- [5] T. R. Shrout, S. J. Zhang, R. Eitel, C. Stringer, C. A. Randall, In 14th IEEE International Symposium on Applications of Ferroelectrics, 2004, ISAF-04. (2004).
- [6] S. Fujii, Y. Shimada, K. Utsumi, Y. Saito, NEC Corp, U.S. Patent **4**(574), 255 (1986).
- [7] R. I. Scott, M. Thomas, C. Hampson, *Journal of the European Ceramic Society* **23**(14), (2003).
- [8] K. Inomata, K. Nakajima, Y. Saito, U.S. Patent **6**(381), 171 (2002).
- [9] M. S. Augsburger, M. C. Viola, J. C. Pedregosa, A. Munoz, J. A. Alonso, R. E. Carbonio, *Journal of Materials Chemistry* **15**(9), (2005).
- [10] L. Ortega-San Martin, J. P. Chapman, L. Lezama, J. Sánchez-Marcos, J. Rodríguez-Fernández, M. I. Arriortua, T. Rojo, *Journal of Materials Chemistry* **15**(1) (2005).
- [11] B. Orayech, L. Ortega-San-Martin, I. Urcelay-Olabarria, L. Lezama, T. Rojo, M. I. Arriortua, J. M. Igartua, *Dalton Transactions* **45**(36), (2016).
- [12] B. Amrithakrishnan, G. Subodh, *Materials Research Bulletin* **93**, (2007).
- [13] S. C. Lal, A. M. Aiswarya, K. S. Sibi, G. Subodh, *Journal of Alloys and Compounds* **788**, (2019).
- [14] M. L. Lopez, I. Alvarez, M. Gaitan, A. Jerez, C. Pico, M. L. Veiga, *Solid State Ionics* **63**, (1993).
- [15] B. H. Toby, *Journal of Applied Crystallography* **43**(5), (2010).
- [16] A. C. Larson, R. B. Von Dreele, General Structure Analysis System (GSAS); Los Alamos National Laboratory LAUR, (2004).
- [17] H. Rietveld, *Journal of Applied Crystallography* **2**(2), (1969).
- [18] R. D. Shannon, *Acta Crystallographica section A: crystal physics, diffraction, theoretical and general crystallography* **32**(5), (1976).
- [19] J. W. G. Bos, J. P. Attfield, *Physical Review B* **70**(17), (2004).
- [20] V. L. Vilesh, G. Subodh, *Ceramics International* **43**(15), (2017)
- [21] S. Anjum, A. Masud, *Digest Journal of Nanomaterials and Biostructures* **13**(4), (2018).
- [22] S. C. Lal, A. Rajan, G. Subodh, *Materials Today: Proceedings* **4**(2), (2017).
- [23] K. Li, H. Lian, R. Van Deun, M. G. Brik, *Dyes and Pigments* **162**, (2019).
- [24] A. E. Lavat, R. C. Mercader, E. J. Baran, *Journal of Alloys and Compounds* **508**(1), (2010).
- [25] M. Liegeois-D., *Spectrochimica Acta Part A: Molecular Spectroscopy* **31**(11) (1975).
- [26] F. Ding, M. L. Nisbet, H. Yu, W. Zhang, L. Chai, P. S. Halasyamani, K. R. Poeppelmeier, *Inorganic Chemistry* **57**(13), (2018).
- [27] J. A. Mydosh, *Spin glasses: an experimental introduction*, CRC Press, p. 120 (2014).
- [28] A. Haldar, K. G. Suresh, A. K. Nigam, *EPL (Europhysics Letters)* **91**(6), (2010).
- [29] M. K. Singh, W. Prellier, M. P. Singh, R. S. Katiyar, J. F. Scott, *Physical Review B* **77**(14), (2008).

- [30] T. Sarkar, M. Motin Seikh, V. Pralong, V. Caignaert, B. Raveau, B., Applied Physics Letters **100**(23), (2012).
- [31] P. Munirajaa, K. S. Kumara, A. Sudharania, M. Ramanadhaa, S. Ramua, R. P. Vijayalakshmia, B. Poornaprakashb, Digest Journal of Nanomaterials and Biostructures **15**(2), (2020).
- [32] M. C. Dimri, H. Khanduri, H. Kooskora, M. Kodu, R. Jaaniso, I. Heinmaa, A. Mere, J. Krustok, R. Stern, Journal of Physics D: Applied Physics **45**(47), (2012).
- [33] H. Trabelsi, M. Bejar, E. Dhahri, M. Sajieddine, M. A. Valente, A. Zaoui, Journal of Alloys and Compounds **680**, (2016).